

UCLA

UCLA Previously Published Works

Title

Ab initio determination of peptide structures by MicroED

Permalink

<https://escholarship.org/uc/item/75k2g7gqz>

ISBN

978-1-0716-0966-8

Authors

Zee, Chih-Te
Saha, Ambarneil
Sawaya, Michael R.
et al.

Publication Date

2021

Peer reviewed



Published in final edited form as:

Methods Mol Biol. 2021 ; 2215: 329–348. doi:10.1007/978-1-0716-0966-8_17.

***Ab initio* determination of peptide structures by MicroED**

Chih-Te Zee¹, Ambarneil Saha¹, Michael R. Sawaya^{2,*}, Jose A. Rodriguez^{1,*}

¹Department of Chemistry and Biochemistry; UCLA-DOE Institute for Genomics and Proteomics; STROBE, NSF Science and Technology Center; University of California, Los Angeles (UCLA); Los Angeles, CA 90095, USA

²Howard Hughes Medical Institute, UCLA-DOE Institute, Departments of Biological Chemistry, Chemistry & Biochemistry, and Molecular Biology Institute, Box 951570, UCLA, Los Angeles, CA 90024-1570, USA

Abstract

Structural elucidation of small macromolecules such as peptides has recently been facilitated by a growing number of technological advances to existing crystallographic methods. The emergence of electron micro-diffraction (MicroED) of protein nanocrystals under cryogenic conditions has enabled the interrogation of crystalline peptide assemblies only hundreds of nanometers thick. Collection of atomic or near-atomic resolution data by these methods has permitted the *ab initio* determination of structures of various amyloid-forming peptides, including segments derived from prions and ice-nucleating proteins. This chapter focuses on the process of *ab initio* structural determination from nano-scale peptide assemblies and other similar molecules.

Keywords

peptide; nanocrystal; amyloid; *ab initio* ; direct methods

1. Introduction

Electron micro-diffraction (MicroED) of macromolecules is a cryoEM technique well-suited to the determination of peptide and small macromolecule structures (1–4). The first novel macromolecular structure solved by MicroED (5), a peptide segment of the Parkinson's-associated protein alpha synuclein, established the method's utility as a means of rapid structural analysis of crystals as small as a hundred nanometers in width. The subsequent determination of four *ab initio* structures of prion peptides demonstrated the approach's expediency in obtaining atomic-resolution structures of peptides (6).

Since these initial breakthroughs, the investigation of peptides by MicroED has grown and now includes 22 structures, including 14 structures at less than or equal to 1.2 Å resolution (3, 7–11). Because of the success of *ab initio* methods for structural determination of peptide assemblies by MicroED (3, 6), we focus this chapter on procedures for the collection of high-resolution MicroED data from peptide nanocrystals and atomic-resolution

*Correspondence to: M.R.S. (sawaya@mbi.ucla.edu) & J.A.R. (jrodriguez@mbi.ucla.edu).

determination of *ab initio* structures from said crystals. This approach hinges on the availability of well-ordered crystals hundreds of nanometers thick and the concurrent use of cryogenic techniques to minimize radiation damage (1). We demonstrate the implementation of this technique on GSNQNNF, a routinely studied heptapeptide segment of the prion protein (12), which forms needle-like crystals several microns in length but no more than a few hundred nanometers thick and wide.

As with the interrogation of larger macromolecular structures by MicroED, data collection from frozen hydrated crystals proceeds by measuring diffraction from a selected area of an illuminated crystal while that crystal is rotated unidirectionally in the electron beam (1, 13). Diffraction movies recorded during this process are then converted into formats accessible to conventional crystallographic processing programs, which reduce MicroED data to intensities (13) used for *ab initio* structural determination by direct methods. Solutions obtained by this approach contain collections of atoms which display correlations with the measured data. These in turn can generate Coulomb potential maps that inform the placement of residues along a polypeptide chain. Fourier difference density in these structures reveals the positions of riding hydrogens, a feat difficult to accomplish via conventional crystallographic methods (5, 6, 14).

The procedures outlined by this chapter assume a certain degree of practical and theoretical knowledge related to operation of transmission electron microscopes, cryoEM, crystallography, and diffraction theory. For a primer on these subjects the reader is encouraged to read additional chapters in this book, or one of several recent reviews or books (1, 15–18).

2. Materials

2.1 Sample-preparation tools and consumables

1. 200 - 400 mesh grids, covered with continuous or perforated carbon.
2. Ultra-fine grade reverse self-closing tweezers.
3. Vitrobot fine-tip tweezers.
4. Whatman No. 1 filter paper for specimen blotting and standard Vitrobot filter paper.
5. Glass petri dish with lid for grid storage and transport.
6. 2, 10, 20 microliter micropipettors for sample manipulation and application.
7. Crystal slurries prepared in batch, as hanging or sitting drop vapour diffusion or other crystal growth and storage system.
8. Cryogen-resistant grid storage boxes with screw-top tool.
9. For safety, several procedures require use of safety goggles, gloves and cryogen protection including cryogen gloves and face shields.

2.2 Grid surface treatment

1. Several surface treatment systems are adequate (19). We describe use of a PELCO easiGlow, glow discharge and plasma generation system capable of plasma current of up to 30 mA, with vacuum control and containing a platform with a recess suited for 25 x 75 mm slide. This equipment also requires a rotary vacuum pump and gas and vent inlets.
2. Clean glass micro-slide, 75 x 25 mm, 1 mm thick with frosted end onto which grids can be placed for glow discharging. Alternatively, a grid holder block can be used instead.

2.3 Cryo storage and Cryo-Transfer systems

1. Several sample vitrification tools are available to perform rapid sample cooling following the Dubochet method (20, 21). Here we describe use of a Vitrobot Mark IV cryosample plunger capable of automated sample vitrification into liquid ethane.
2. While a number of sample transfer holders are available, we describe use of the Gatan 626 cryo transfer holder with a high tilt range and low sample drift.
3. The Gatan cryo transfer holder pairs with a Gatan dry pumping station model 655 and Gatan cryo transfer station.

2.4 Microscope Components

1. Microscope types include Tecnai series FEI microscopes such as F20 TEM (200 keV) (13), F30 TEM (300 keV) (22), FEI Talos Arctica S/TEM (200 keV) (4) or Titan (300 keV), or JEOL JEM-3200, JEM-2200/2100 or cryo ARM series (23). Here we describe use of a Tecnai F30 TEM (300 keV) in microprobe mode.
2. Electron source: Field emission gun operating with accelerating voltages in the 100-300 keV range. (*see Note 1*)
3. Selected area aperture: Aperture diameters in the 50-150 micrometer range are recommended; depending on lens system, aperture sizes corresponding to 0.5-4.0 micrometers in diameter at the image plane.
4. Sample stage: Stage accuracy tilt range and tilt speed should be carefully calibrated to maintain eucentricity at the sample. Tolerance limits of stage accuracy, 0.1°; tilt range of ± 70°, tilt speed of 0.1-10° per second.

¹-Recommended instruments employ Schottky-type field-emission guns (FEGs) as electron sources. These contain elemental tungsten (W) tips roughly 15 nm in diameter coated with a thin layer of zirconium oxide (ZrO). The apex of the emitter approaches 1800 K during excitation, augmenting ZrO conductivity and facilitating thermionic emission by diminishing the work function of the cathode. Schottky-type FEGs generate a highly coherent beam, with an energy spread ΔE of 0.3-0.7 eV. Alternative sources such as W hairpin filaments or lanthanum hexaboride crystals exhibit ΔE values of 1.5-3 eV and 1-2 eV, respectively. Systems operating at a higher accelerating voltage are preferred since these can also accommodate lower accelerating voltages (i.e., a 300 keV instrument can be driven at 200 keV if necessary). Although so-called “cold FEGs” (in instruments such as the JEOL JEM-2100) can achieve even better spatial coherence, Schottky-type FEGs offer greater durability, lower noise, and steadier beam current (34).

2.5 Cameras and computing

1. Several detectors are suitable for data collection including some that have been developed specifically for MicroED. We focus on use of the TVIPS TemCam-XF416 with a 16-megapixel CMOS sensor with integrated electronics delivering 16-Bit images at up to 48 frames per second with correlated double sampling (22). (*see Note 2*)
2. The camera is controlled by EMMenu4 with two pre-set camera recording settings. The first at full-chip readout with subsampling by 2, the second with full-chip readout with subsampling by 4; both in rolling shutter mode.
3. Computing infrastructure is essential for both data collection and processing. Here we describe software operating in a Linux environment on a server system powered by 40 processing threads (Intel® Xeon® CPU E5-2680 v2 @ 2.80 GHz) with 256 GB of RAM and connected to a storage server with 400 TB of redundant (RAID6) NFS storage.

2.6 Data reduction and structure determination software

1. Data parsing and diffraction visualization software: Software for conversion of diffraction movies to crystallographic format diffraction images is limited. We describe conversion of Tietz Video Image Processing (TVIPS) files to SMV format using a custom program: tvips2smv (<https://cryoem.ucla.edu/pages/MicroED>) (13). Diffraction image visualization can be achieved using the Adxv program (www.scripps.edu/tainer/arvai/adxv.html) that reads SMV files (24).
2. Data processing programs (*see Note 3*): Indexing, integration, merging, and scaling can be achieved through a variety of software programs. We describe use of the XDS package (<http://xds.mpimf-heidelberg.mpg.de/>) (25).
3. *Ab initio* structure determination is achieved using various direct methods programs. We describe use of the SHELX-97 suite, programs SHELXD and SHELXT (<http://shelx.uni-ac.gwdg.de/>) (26).
4. X-ray crystallographic refinement programs suitable for processing electron diffraction data must have the capacity to use electron scattering factors. Among those described here are the SHELX-97 suite (26); Phenix Suite (<https://www.phenix-online.org/>) (27); CCP4 suite: REFMAC (<http://www.ccp4.ac.uk/>) (28).
5. Several programs are available for dataset visualization, model building, and structural analysis: The ViewHKL program in the CCP4 suite can be used for

²Other detectors include the CMOS-based CetaD 16M (Thermo Fisher Scientific, (35)), a previous generation TVIPS TemCam-F416 (Tietz Video and Image Processing, (13)), and two direct electron detectors, Falcon in integrating mode (35) and K2 in counting mode (Gatan Inc., (36)). Hybrid pixel detectors such as the Dectris EIGER detector (37) and the Medipix2 (38) allow for fast and high dynamic range data collection. In principle, collection of MicroED data using a slow-scan CCD is possible, but inherent deficits in readout speed may severely limit data quality.

³Because continuous rotation of the sample stage during MicroED is partially analogous to rotation of a mounted crystal on an X-ray diffractometer, software originally developed for X-ray crystallography can also process MicroED data. However, numerous parameters and settings (e.g. the wavelength of the incident radiation and the values of the relevant atomic scattering factors) must be adjusted accordingly to account for the discrepancies between X-rays and electrons.

dataset visualization (29), the Coot model building program (<https://www2.mrc-lmb.cam.ac.uk/personal/pemsley/coot/>) (30), and PyMOL (<https://pymol.org/2/>) for model building and structure analysis (31).

3. Methods

This section provides guidance on the experimental workflow of electron diffraction from peptide nano- and microcrystals, from sample preparation to structure determination (Fig. 1).

3.1 Grid preparation and freezing (see Note 4)

1. Transfer EM grid from box to a clean glass slide using ultra-fine self-closing tweezers.
2. Glow discharge grid for 20-60 seconds per side at 28–30 mA, following manufacturer's instructions.
3. Prepare Vitrobot for freezing following manufacturer's instructions, filling the sample storage reservoir with liquid nitrogen, placing a grid storage box in the liquid nitrogen reservoir, placing the copper ethane cup at its center and linking them via a heat transfer apparatus. Condense ethane into cup following safety protocols (see Note 5).
4. Secure grid using Vitrobot tweezers and place into Vitrobot assembly following manufacturer's instructions, as per the Dubochet method (21).
5. Collect 5 microliters or more of a slurry of crystal fragments of sub-micron thickness suspended in mother liquor.
6. Place 1-3 microliters of crystal slurry per side, on either one or both sides of the grid (see Note 6).
7. Immediately follow Vitrobot procedures for blotting and plunge freezing of grid into liquid ethane (32) (see Note 7), then transfer the grid to liquid nitrogen storage box.

⁴To avoid redundancy, we minimize our description of procedures that may be more extensively covered by other chapters. Please refer to other chapters in this volume for a more thorough explanation of these topics and/or procedures.

⁵Due to liquid nitrogen's relatively low heat capacity, samples plunge-frozen in liquid nitrogen often suffer from co-crystallization of adventitious ice. This is because interaction with the room-temperature sample causes an insulating layer of nitrogen to evaporate immediately upon contact as described by the Leidenfrost effect, prolonging the flash-freezing process and allowing water sufficient time to crystallize. Conversely, liquid ethane exhibits much higher heat capacity and therefore functions as a ruthlessly efficient cryogen that captures samples in vitreous ice. However, this property also renders it far more hazardous. Liquid ethane causes severe cryogenic burns immediately upon contact with exposed skin. When condensing ethane, exercise extreme caution and wear appropriate personal protective equipment, such as long cryogenic gloves, at all times.

⁶Certain types of EM grids exhibit incompatibility with particular solvents. For example, formvar, a common plastic support film, is soluble in chloroform, dichloroethane, and 1,4-dioxane. Also, copper and some other metal meshes are highly susceptible to degradation by acids and bases.

⁷Choice of cryo-protectants can increase the difficulty of an experiment by obstructing blotting efficiency. In general, an evaluation of solvent choice and sample compatibility with grids and freezing conditions prior to sample deposition is critical. For example, certain materials routinely used in X-ray diffraction can be incompatible with conventional sample preparation for MicroED. Common, non-volatile cryoprotectants (such as paratone oil, sucrose, trimethylamine *N*-oxide (TMAO), lepidic cubic phases, and perfluoropolyether oils) can cause particular challenges for both freezing and sample interrogation by an electron beam.

8. Transfer grid boxes to permanent storage or to cryo holder transfer station for immediate use.

3.2 Cryo-Transfer (see Note 4)

1. Cool cryo transfer station with liquid nitrogen following manufacturer's instructions and transfer sample grid box containing sample grids into the transfer station sample platform.
2. Having followed procedures for preparation of the 626 cryo-transfer holder - in particular the performance of a bakeout of the zeolite in the holder vacuum chamber - remove the holder from the 655 pumping station following manufacturer's instructions and place into the cryo transfer station.
3. Fill sample holder dewar with liquid nitrogen and refill transfer holder station with liquid nitrogen to the level of the holder bar. Pull back protective copper blades to allow sample placement onto holder.
4. Remove grid from sample box and place onto sample holder with pre-cooled fine tip tweezers.
5. Place copper clip ring on top of grid and secure onto sample holder, cover sample with protective blades.
6. Remove transfer holder from station and place into microscope compustage at the correct orientation, making sure to minimize the amount of time the holder spends in air.

3.3 Grid screening and preliminary diffraction

1. Assuming operation of a fully calibrated instrument in microprobe mode, perform eucentric height alignment by wobbling of the sample and adjusting the *z*-height.
2. Focus the system on the back focal plane of the objective lens by adjusting the focus knob at a magnification greater than 15,000 when viewing the edge of a hole or a distinctive feature on the carbon support.
3. Return magnification to 5,800, expand the beam using the intensity knob to a desired value and set spot size to 11. (see Note 8)
4. Press diffraction button on console to operate the microscope in diffraction mode and ensure the beam is free of astigmatism (see Note 9).
5. The beam focus can be changed by adjusting the defocus knob on the console at the desired detector distance and C2 lens intensity. Position the beam at the

⁸Generally, expansion of the beam beyond the central circle of the fluorescent screen at 5800x magnification is desired. Ultimately, the size of the beam will determine the flux on the sample in electrons per Ångstrom squared. An image of the electron beam propagating through vacuum can help estimate the dose at low electron counts.

⁹To calibrate the diffraction stigmator, adjust the C2 lens intensity. A fully condensed beam sits at a crossover point: adjusting the C2 intensity in either direction should result in an expansion. The beam should expand and collapse concentrically as a nearly circular ellipse. Shape distortions should be corrected by adjusting the console multifunction knobs while the stigmator adjustment icon is active.

center of the detector and calibrate the location of the selected area aperture (SAA) as needed.

6. For sample detection, expand the beam by adjusting the power to the condenser lens used to focus the beam. This can be achieved, for example, by turning the intensity knob to enter overfocused diffraction mode. One could pre-set this configuration using low-dose settings. Scan and scan the grid for crystals by moving the stage x , y location using the trackball or joystick. If available, low dose mode can automate the focus adjustments to minimize electron exposure on samples while the grid is examined. Where low dose is available, visual inspection of the grid can be performed in overfocused diffraction under the ‘focus’ or ‘search’ mode, while diffraction patterns can be recorded with the beam at crossover in ‘exposure’ mode on an FEI microscope.
7. Find an appropriate object on the grid to use as a reference and fine-tune the specimen’s eucentric height by adjusting the z -height while wobbling.
8. Diffract from a target crystal by I) inserting the SAA; II) inserting and adjusting the beamstop; III) returning the beam to a condensed state by adjusting the intensity; IV) capturing an initial diffraction pattern with an exposure ranging from 0.1 to 10 seconds (see Note 10); V) repeating steps I-IV as necessary to (1) assess the resolution to which the sample appears to diffract and (2) diagnose whether or not this particular crystal diffracts well enough to warrant collection of a full dataset.
9. Verify if the detector distance is appropriate for sample and adjust if necessary, using the magnification knob. (see Note 11)
10. Fine-tune the z -axis height in overfocused diffraction mode while tilting the sample between the upper and lower limits planned for data collection. The crystal should always remain within the SAA throughout the desired tilt range. (see Note 12)
11. To collect diffraction movies as the stage rotates from one high angle tilt to the other, initiate data recording on the camera while independently setting a stage trajectory at a desired rotation rate. (see Note 13)

¹⁰While the XF416 detector is capable of full-chip readout at nearly 50 frames per second, not all applications warrant this readout speed. In particular, certain applications such as shutter-free data collection may benefit from slower readouts that limit the accumulation of readout noise. Likewise, spatial subsampling or binning of the collected frames can enhance signal over noise. The collection strategies described here rely on 2x2 binning of full-frame diffraction images, but larger binning can be employed if desired, with a caveat. Binning reduces sampling of the reciprocal lattice and therefore constrains measurements as lattice spacings shrink and reflections risk being overlapped. This is also influenced by the selected camera length as described in the following note.

¹¹The ideal detector distance places the finest-resolution reflections at or near the edge of the detector, maximizing the collection of reflections at both coarse- and fine-resolution shells. Crystals with larger unit cell dimensions will exhibit a more compact reciprocal lattice and require longer detector distances to prevent overlapping spots from affecting integrated intensities. This is influenced by detector sampling of the reciprocal lattice.

¹²Visual obstruction of the sample by grid bars, other crystals, or debris is commonplace at high tilts, effectively limiting the upper and lower bounds of rotation. Keep in mind that as the x - and y -axes approach the stage’s outer boundaries, high-angle tilts become more likely to cause physical collisions between the microscope and the sample holder.

¹³Coordination of stage rotation with diffraction data collection requires manual intervention. The software module controlling stage rotation can be accessed through the Temspy dialog box, under dialogues, CompuStage. The parameters for saving recorded movies can be set by accessing the Recorder Settings dialog box from the toolbar menu. Video capture occurs by pressing the camcorder icon

12. Repeat step 11 for subsequent data collection from different samples. (*see* Note 14)

Sections 3.4 to 3.6 provide detailed instructions to execute data processing with select software programs (Fig. 3).

3.4 Data conversion and processing

1. Use a script such as `twips2smv` to convert raw movie files from native ‘.twips’ format (Tietz Video and Image Processing Systems, generic output from TemCam detectors) or other proprietary format into a series of images in standard crystallographic format (e.g. SMV, with a ‘.img’ suffix) readable by XDS. Before executing conversion, specify the oscillation range and detector distance used for the dataset in the command line (13).
2. Visualize the images using `Adxv` to cycle through the converted frames. Select an appropriate image to use for identification of the beam center. (*see* Note 15) Repeat this process on several different images to obtain a more precise value.
3. Generate or download an appropriate XDS input template (http://xds.mpimf-heidelberg.mpg.de/html_doc/xds_prepare.html).
4. To specify the location of the beam center in a dataset, use the values calculated in step 2 as the inputs for origin parameters in the XDS.INP file.
5. Enter the correct relativistic wavelength of the incident electron beam as the X-RAY_WAVELENGTH. This parameter is dependent on the specific accelerating voltage employed by the instrument. (*see* Note 16)

on the EMMenu4 user interface having set a desired integration time per frame. A second icon (red record button on the EMMenu4 user interface) allows for storage of the captured video frames when pressed as video is being captured.

¹⁴To achieve optimal data quality, parameters such as camera length, continuous rotation rate, exposure time and crystal orientation must be judiciously selected. A rotation rate of 0.1 to 0.5 degrees per second is recommended. Faster oscillations may result in overlapping spots, while slower oscillations may result in an insufficient number of spots due to sample degradation over time. Additionally, exposure times between 0.1-10 seconds are recommended. Longer exposures can increase the signal-to-noise ratio, but may place reflections from large unit cells in danger of overlapping, even at slow oscillations. Data from crystals that demonstrate orientation bias when deposited on a grid is limited in its sampling of reciprocal space (i.e., via collection of diffraction patterns at high tilt). Sufficient sampling is critical for obtaining high completeness data.

¹⁵Several procedures exist for identifying the location of the beam center in a diffraction image. We describe a procedure based on the relationship between the approximate locations of Friedel mates. Here, one would draw lines connecting pairs of Friedel mates to estimate the spatial coordinates of the beam center. The position of the beam center may change or drift between or within datasets. If this occurs, re-calculate its value accordingly.

¹⁶XDS requires the user to supply the wavelength of the incident radiation. While this is denoted X-RAY for historical reasons, its name has no bearing on the calculations performed by the program. Calculation of this key parameter is straightforward for X-rays (characteristic values include 0.7107 Å for Mo K α and 1.5418 Å for Cu K α). In contrast, typical TEM accelerating voltages (i.e., >100 keV) suitable for MicroED produce a high-energy beam in which each constituent electron is forcibly propagated through a potential drop, ultimately producing a beam of quanta traveling at a velocity greater than half the speed of light. Therefore, an accurate calculation of the electron wavelength must incorporate relativistic contraction, as follows:

$$\lambda = \frac{h}{\sqrt{2m_0eV\left(1 + \frac{eV}{2m_0c^2}\right)}}$$

In the above equation, h is Planck’s constant, m_0 is the rest mass of the electron, eV is the kinetic energy imparted by the accelerating voltage, and c is the speed of light in a vacuum. See Table 1 for characteristic values for the relativistic wavelength of the incident electron beam, which include 0.0251 Å at 200 keV and 0.0197 Å at 300 keV (34). Discrepancies between the relativistic

6. Enter the correct ROTATION_AXIS values according to the direction of rotation and predetermined detector geometry, which differs by instrument.
7. Based on a visual inspection of the stack of diffraction images in Adxv, pinpoint the specific range of frames which incorporates the highest-quality data to be used for indexing. Set SPOT_RANGE as this set of frames. Omit frames with visible defects such as polycrystalline reflections or overly elongated, ellipsoidal spots. DATA_RANGE specifies the range of images used for integration and can include all the frames specified in SPOT_RANGE and more.
8. Run XDS. If no errors occur, proceed to step 9. If errors appear, see Note 17.
9. The stringency of IDXREF may result in the frequent appearance of errors associated with lattice determination, prematurely halting further processing. If confidence in the lattice type is high, the error can be circumvented by modifying the JOB settings in the XDS.INP input file as suggested by the error output and rerunning XDS. (*see* Note 18)
10. Optimize the indexing solution by adjusting parameters such as the set of frames used for indexing and integration, the minimum number of pixels in a peak, the thresholds for background and peak pixel selection, and the mosaicity model. (*see* Note 19)
11. Run XSCALE on the optimized indexing solution.
12. Repeat steps 1-10 for each movie collected.

3.5 Data set merging

1. To merge datasets, create a new XSCALE.INP input file.
2. Specify the respective file paths of each desired XDS_ASCII.HKL file using INPUT_FILE. (*see* Note 20)

and non-relativistic calculations widen significantly as the accelerating voltage rises. Furthermore, recall that the radius $1/\lambda$ of the corresponding Ewald sphere scales inversely with the wavelength of the incident quanta. As a result, given the markedly shorter wavelengths inherent to electron diffraction, the curvature of the Ewald sphere is flattened, and its gently sloping arc is reliably approximated as a plane at >100 keV. (This stands in stark contrast to X-ray diffraction, in which the geometry of the Ewald sphere stays true to its name.) Each observed reflection represents a cross-section between the surface of the Ewald sphere and a reciprocal lattice vector. Therefore, a wide, flattened Ewald sphere can in principle accommodate many reciprocal lattice points per angle. In practice, this advantage is attenuated by the restricted tilt range available to TEM instruments.

¹⁷If IDXREF produces an error beginning with “INSUFFICIENT PERCENTAGE (< 50%) OF INDEXED REFLECTIONS,” proceed to step 9. If XDS fails to find an adequate indexing solution (“IER=0”), inspect the values for the parameters set in steps 3-5. Specifically, consider supplying a different range of frames for SPOT_RANGE. If XDS cannot determine an adequate indexing solution after multiple iterations of adjustments, it may indicate poor data quality.

¹⁸The IDXREF error described in Note 17 may be caused by many factors, including a limited tilt range. Unlike a multi-axis goniometer, TEM instruments exhibit a restricted range of motion. Thus, MicroED datasets may not always include a large number of reflections within a given wedge of reciprocal space, leading to indexing ambiguities. Other potentially causative factors include non-eucentric sample rotation and lens aberrations (18).

¹⁹Statistical analysis of each processing task implemented by XDS (such as IDXREF, etc.) is stored in its respective log file (with an ‘.LP’ extension, such as IDXREF.LP). These log files contain a preponderance of potentially useful information which could enhance or facilitate an indexing solution. As an illustrative example, CORRECT.LP supplies detailed statistics describing several alternative solutions generated by indexing smaller subsets of frames within the previously specified SPOT_RANGE. This provides insight into which specific set of frames is truly ideal for SPOT_RANGE.

²⁰Due to hardware restrictions imposed by the instrument, individual MicroED datasets rarely yield sufficiently high values of overall completeness to generate tractable direct-methods solutions on their own. Merging several datasets can compensate for this. For n independent datasets, there exist $2^n - 1$ unique ways to exhaustively merge them together. Note that XSCALE can also truncate each individual dataset at a given resolution range using INCLUDE_RESOLUTION_RANGE. Only select individual datasets that generate

3. Run XSCALE. Analyze the statistics of the merged solution in XSCALE.LP. (*see* Note 21) (Fig. 4A)
4. Once a satisfactory merge is successfully implemented, open XDSCONV.INP and set the output type and file extension to SHELX and '.hkl', respectively.
5. Run XDSCONV to convert the scaled reflection file generated by XSCALE (with an '.ahkl' extension) to '.hkl' format. This renders it readable by SHELX.
6. Alternatively, open XDSCONV.INP and set the output type and file extension to CCP4_I+F and '.ascii', respectively. Run XDSCONV. XDSCONV will prompt the user for additional lines of commands to be copied and pasted, generating a binary list of reflections with the extension '.mtz'.
7. Visualize the '.mtz' file (Fig. 4B) with viewHKL and search for systematic absences to aid in space group determination.

3.6 Structure determination

1. Generate a SHELX instruction file (extension '.ins') by using SHELXPRO (26) (*see* Note 22).
2. Execute SHELXD/T with the newly made instruction file and the list of reflections generated in step 5 in the previous section ('.hkl'). During the SHELX trials, keep track of the best CFOM values; these form a distribution indicative of correct solutions (Fig. 5). (*see* Note 23)
3. Open the direct methods solution in Coot ('.pdb' or '.res' files tolerated) or PyMOL (accepts '.pdb' files) to visualize the atoms. Generally, a solution is considered valid when each atom in the polypeptide backbone is placed in accordance with well-established restraints on bond geometries (Fig. 6A).
4. While structure determination programs do not routinely assign the absolute configuration of individual stereocenters from electron diffraction data, special routines can be implemented to exploit potential differences in Friedel mates

highly convergent indexing solutions (i.e., datasets which exhibit strong agreement in parameters such as unit cell dimensions, Laue symmetry, etc.). Forcibly merging inherently discordant datasets will undeniably prove fruitless.

²¹Obtaining an optimal dataset may require systematic screening of parameters (i.e., adjusting resolution range, re-indexing individual movies, merging disparate combinations of movies, etc.) to improve statistics. Attempt to minimize R-factors and maximize completeness and I/SIGMA. For an example of the summary statistics produced by XSCALE, see Figure 4.

²²Many methods exist for generating instruction files for SHELXD. For example, a custom program (referred to here as shelxdpro) can facilitate direct methods solutions of protein/peptide structures. To achieve this, shelxdpro prompts users for information needed to generate instruction files for running SHELXD or SHELXT. First, shelxdpro prompts the user to enter the protein sequence, the space group number, and the unit cell parameters. Shelxdpro uses this information to calculate Matthews coefficients and suggest feasible choices for the number of molecules in the asymmetric unit. The user selects a value, and then shelxdpro calculates the number of carbons, nitrogens, oxygens, and other atoms required to write the SFAC, UNIT, FIND, and PLOP statements. Lastly, shelxdpro asks for the name of the SHELX formatted diffraction data file (.hkl) for this project and an indication of whether the file contains amplitudes or intensities. Shelxdpro writes this information, including space group operators in a format that SHELXD/T accepts. The user can use this instruction file to run shelxd/t immediately. The benefit of such a program is time savings in omitting a search inputs such as space group operators and number of atoms of each element in the unit cell. Such a program also relieves the user of remembering the cryptic lattice code specific to the space group and eliminates the possibility for formatting errors.

²³SHELXD requires the user to supply an exact space group for direct methods and is therefore unlikely to yield a reasonable solution if the user's prediction is incorrect. Conversely, SHELXT extracts the Laue symmetry of the indexing solution and determines the space group through multiple considerations (39). Depending on the number of atoms, solutions with a combined figure of merit (CFOM) greater than 80 will have a high probability of being correct (Fig. 5).

(33). In the event that absolute structure is known but SHELXD/T outputs its inverse, the PDBSET program (29) can rectify the handedness of the coordinate file by inverting the input coordinates.

5. SHELXL can use the original list of reflections and the atomic coordinates output by SHELXD/T to generate an electron density map for model building. Make a copy of the '.res' output from SHELXD/T and rename it as an '.ins' file. Now rename the '.hkl' file used for direct methods calculations so that it matches the new '.ins' file. Run SHELXL, calling the new '.ins' and '.hkl' files as inputs. This will produce a calculated electron density map as an '.fcf' file (also readable in Coot).
6. Build a polypeptide model in Coot or PyMOL by sequentially assigning specific residues according to the data (Fig. 6B).
7. Refine the structure using the newly built model in tandem with the original list of reflections ('.hkl') supplied by XDSCONV in step 5 of section 3.5. Several standard programs can execute refinement; Phenix, REFMAC and Jana natively support electron scattering factors. (*see* Note 24)

Acknowledgements:

We thank Drs. Duilio Cascio, Marcus Gallagher-Jones and Ms. Lee Joon Kim (UCLA) for careful reading of this chapter and for their insightful comments and discussion. This work is supported by the STROBE National Science Foundation Science & Technology Center, Grant No. DMR-1548924, DOE Grant DE-FC02-02ER63421 and NIH-NIGMS Grant R35 GM128867. A.S. is supported as an NSF Graduate Research Fellow under Grant No. DGE-1650604. J.A.R. is supported as a Searle Scholar, a Pew Scholar, and a Beckman Young Investigator.

References

1. Shi D, Nannenga BL, de la Cruz MJ, et al. (2016) The collection of MicroED data for macromolecular crystallography. *Nat Protocols* 11:895–904 [PubMed: 27077331]
2. Shi D, Nannenga BL, Iadanza MG, et al. (2013) Three-dimensional electron crystallography of protein microcrystals. *Elife* 2:e01345 [PubMed: 24252878]
3. Rodriguez JA, Eisenberg DS, and Gonen T (2017) Taking the measure of MicroED. *Curr Opin Struct Biol* 46:79–86 [PubMed: 28648726]
4. Jones CG, Martynowycz MW, Hattne J, et al. (2018) The CryoEM Method MicroED as a Powerful Tool for Small Molecule Structure Determination. *ACS Cent Sci* 4:1587–1592 [PubMed: 30555912]
5. Rodriguez JA, Ivanova MI, Sawaya MR, et al. (2015) Structure of the toxic core of α -synuclein from invisible crystals. *Nature* 525:486–490 [PubMed: 26352473]
6. Sawaya MR, Rodriguez J, Cascio D, et al. (2016) Ab initio structure determination from prion nanocrystals at atomic resolution by MicroED. *PNAS* 201606287
7. Zee C, Glynn C, Gallagher-Jones M, et al. (2019) Homochiral and racemic MicroED structures of a peptide repeat from the ice-nucleation protein InaZ. *IUCrJ* 6
8. Gallagher-Jones M, Glynn C, Boyer DR, et al. (2018) Sub-ångström cryo-EM structure of a prion protofibril reveals a polar clasp. *Nat Struct Mol Biol* 25:131–134 [PubMed: 29335561]
9. de la Cruz MJ, Hattne J, Shi D, et al. (2017) Atomic-resolution structures from fragmented protein crystals with the cryoEM method MicroED. *Nat Methods* 14:399–402 [PubMed: 28192420]

²⁴Programs such as SHELXLE require manual input of electron scattering factors as SFAC commands (40). Due to artefacts (such as dynamical scattering) unique to electron diffraction, the R-factors of refined MicroED structures generally exceed those of their X-ray counterparts. An acceptable solution could exhibit R_{work} and R_{free} values near or less than 0.25, with a split below 0.05 (Fig. 6B).

10. Guenther EL, Cao Q, Trinh H, et al. (2018) Atomic structures of TDP-43 LCD segments and insights into reversible or pathogenic aggregation. 25:463–471 [PubMed: 29786080]
11. Hughes MP, Sawaya MR, Boyer DR, et al. (2018) Atomic structures of low-complexity protein segments reveal kinked β sheets that assemble networks. *Science* 359:698–701 [PubMed: 29439243]
12. Hattne J, Shi D, Glynn C, et al. (2018) Analysis of Global and Site-Specific Radiation Damage in Cryo-EM. *Structure* 26:759–766.e4 [PubMed: 29706530]
13. Hattne J, Reyes FE, Nannenga BL, et al. (2015) MicroED data collection and processing. 71:353–360
14. Palatinus L, Brázda P, Boullay P, et al. (2017) Hydrogen positions in single nanocrystals revealed by electron diffraction. 355:166–169
15. Zou X, Hovmöller S, and Oleynikov P (2011) *Electron Crystallography: Electron Microscopy and Electron Diffraction*, Oxford University Press
16. Zuo JM and Spence JCH (2017) *Advanced Transmission Electron Microscopy: Imaging and Diffraction in Nanoscience*, Springer-Verlag, New York
17. Frank J (2006) *Three-Dimensional Electron Microscopy of Macromolecular Assemblies: Visualization of Biological Molecules in Their Native State*, Oxford University Press
18. Heidler J, Pantelic R, Wennmacher JTC, et al. (2019) Design guidelines for an electron diffractometer for structural chemistry and structural biology. *Acta Cryst D* 75:458–466
19. Passmore LA and Russo CJ (2016) Specimen Preparation for High-Resolution Cryo-EM. *Meth Enzymol* 579:51–86
20. Knapik E and Dubochet J (1980) Beam damage to organic material is considerably reduced in cryo-electron microscopy. *Journal of Molecular Biology* 141:147–161 [PubMed: 7441748]
21. Dubochet J, Adrian M, Chang J-J, et al. (1988) Cryo-electron microscopy of vitrified specimens. 21:129–228
22. Jones C, Asay M, Kim LJ, et al. (2019) Characterization of reactive organometallic species via MicroED.
23. Yonekura K, Ishikawa T, and Maki-Yonekura S (2019) A new cryo-EM system for electron 3D crystallography by eEFD. *Journal of Structural Biology* 206:243–253 [PubMed: 30928615]
24. Arvai A (2015) Adxv - A Program to Display X-ray Diffraction Images,
25. Kabsch W (2010) XDS. 66:125–132
26. Sheldrick GM (2008) A short history of SHELX. 64:112–122
27. Adams PD, Afonine PV, Bunkóczi G, et al. (2010) PHENIX: a comprehensive Python-based system for macromolecular structure solution. 66:213–221
28. Murshudov GN, Skubák P, Lebedev AA, et al. (2011) REFMAC 5 for the refinement of macromolecular crystal structures. 67:355–367
29. Winn MD, Ballard CC, Cowtan KD, et al. (2011) Overview of the CCP4 suite and current developments. *Acta Crystallogr D Biol Crystallogr* 67:235–242 [PubMed: 21460441]
30. Emsley P, Lohkamp B, Scott WG, et al. (2010) Features and development of Coot. *Acta Crystallogr D Biol Crystallogr* 66:486–501 [PubMed: 20383002]
31. Delano W The PyMOL Molecular Graphics System, Schrödinger LLC
32. Grassucci RA, Taylor DJ, and Frank J (2007) Preparation of macromolecular complexes for cryo-electron microscopy. *Nat Protocols* 2:3239–3246 [PubMed: 18079724]
33. Brázda P, Palatinus L, and Babor M (2019) Electron diffraction determines molecular absolute configuration in a pharmaceutical nanocrystal. 364:667–669
34. Reimer L and Kohl H (2008) *Transmission Electron Microscopy: Physics of Image Formation*, Springer-Verlag, New York
35. Hattne J, Martynowycz MW, and Gonen T (2019) MicroED with the Falcon III direct electron detector. 615484
36. Gallagher-Jones M, Ophus C, Bustillo KC, et al. (2019) Nanoscale mosaicity revealed in peptide microcrystals by scanning electron nanodiffraction. *Commun Biol* 2:26 [PubMed: 30675524]

37. Tinti G, Fröjdh E, van Genderen E, et al. (2018) Electron crystallography with the EIGER detector. *IUCrJ* 5:190–199
38. Nederlof I, van Genderen E, Li Y-W, et al. (2013) A Medipix quantum area detector allows rotation electron diffraction data collection from submicrometre three-dimensional protein crystals. *69*:1223–1230
39. Sheldrick GM (2015) SHELXT - integrated space-group and crystal-structure determination. *Acta Crystallogr A Found Adv* 71:3–8 [PubMed: 25537383]
40. Peng L-M (1999) Electron atomic scattering factors and scattering potentials of crystals. *Micron* 30:625–648
41. Transmission Electron Microscopy - A Textbook for Materials Science | Williams David B. | Springer, <https://www.springer.com/us/book/9780387765006>
42. Yeates TO and Kent SBH (2012) Racemic Protein Crystallography. 41:41–61

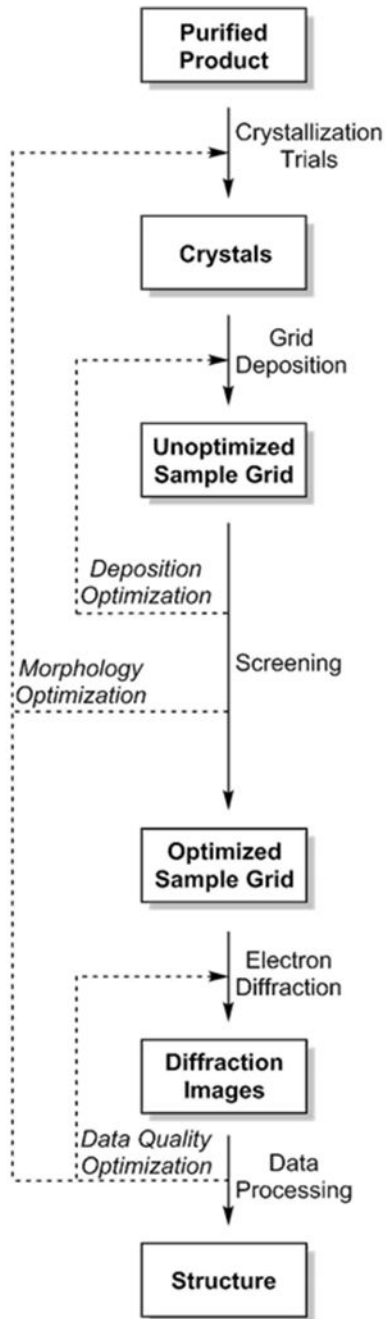


Figure 1. General workflow of experiments to prepare samples, collect diffraction patterns, and process data for structure determination.

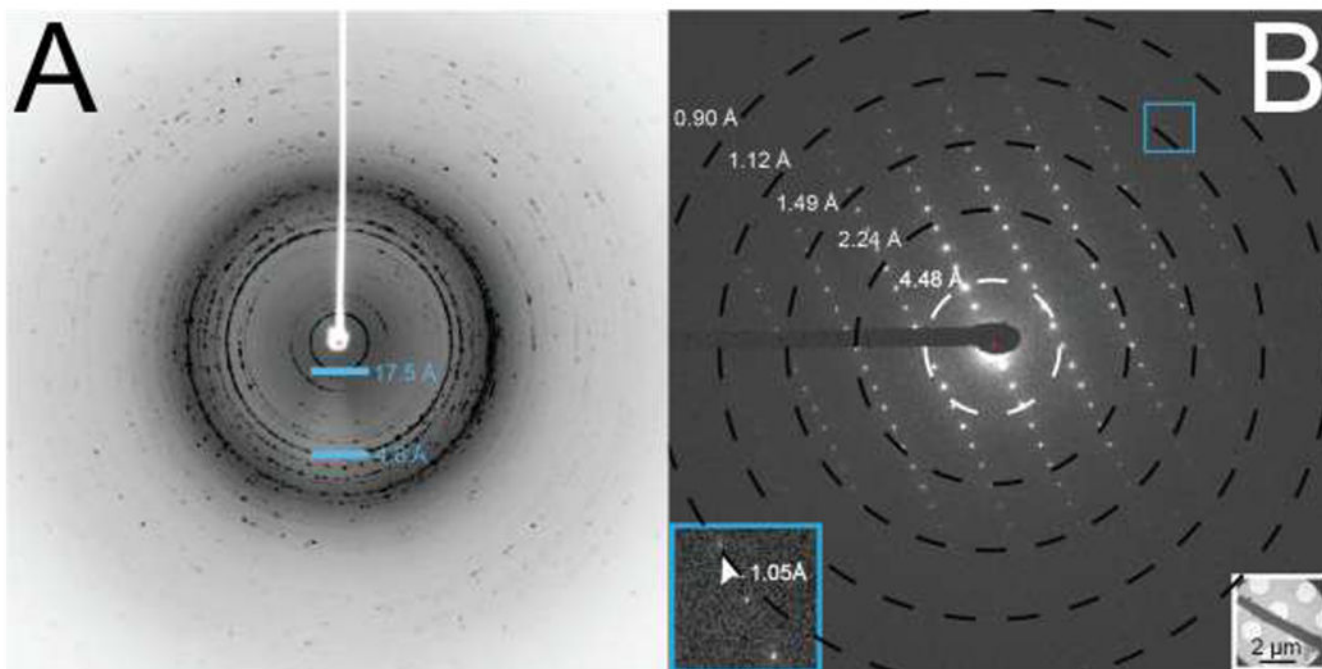


Figure 2.

X-ray powder diffraction (A) and single crystal diffraction pattern (B) of L-GSNQNNF (unit cell dimensions: $a = 4.86 \text{ \AA}$, $b = 14.12 \text{ \AA}$, $c = 17.71 \text{ \AA}$) measured by traditional X-ray diffraction and continuous-rotation MicroED, respectively. The powder diffraction in A integrates a 5° scan of a loop filled with small crystals. Powder diffraction patterns which show gradual radial decay of signal in high-resolution regions suggest the presence of crystalline material, even if certain unit cell vectors lack an intense, corroborating ring. The pattern in B samples a 0.6° wedge of reciprocal space. Blue squares correspond to magnified regions of the pattern showing diffraction between 1.0 and 1.2 \AA . White inset shows the overfocused image of the crystal irradiated to produce the diffraction pattern.

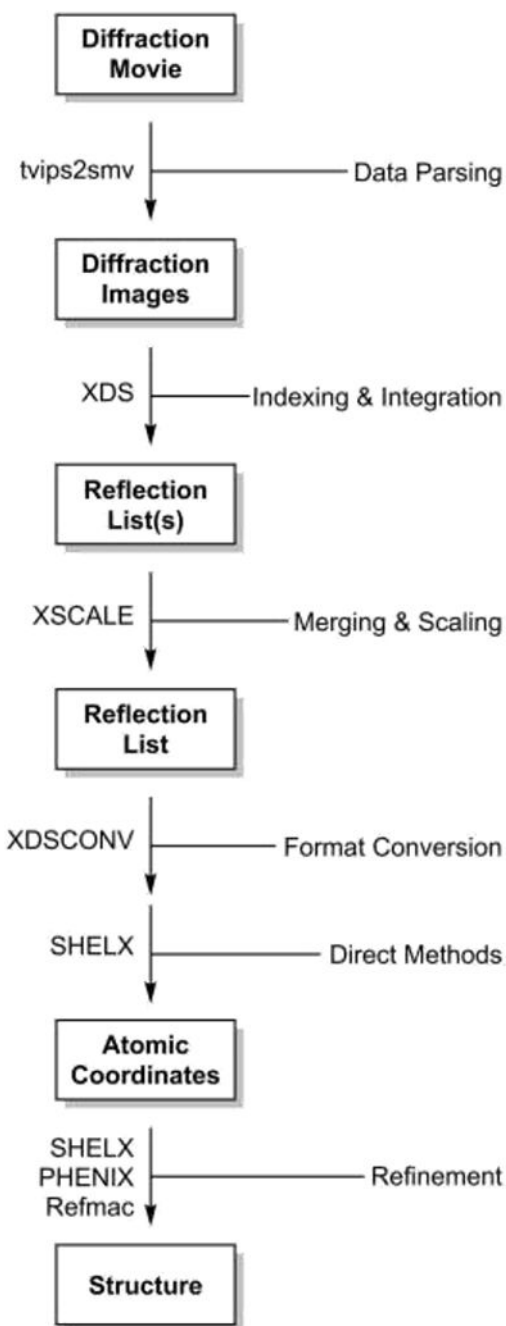


Figure 3. Sample workflow for structure determination *via* direct methods. Section 3.3 covers diffraction; 3.4 covers indexing and integration; 3.5 covers merging, scaling, and format conversion; 3.6 covers direct methods and refinement.

A

Resolution Limit	Number of Reflections			Completeness	R-Factor	I/Sigma	CC(1/2)
	Observed	Unique	Possible				
5.00	15	6	15	40.0%	11.7%	8.72	97.6
3.00	313	67	79	84.8%	11.5%	11.66	97.3
2.00	713	177	220	80.5%	12.6%	9.89	98.0
1.50	1411	341	421	81.0%	13.4%	9.09	96.9
1.40	590	141	173	81.5%	15.5%	7.72	96.7
1.30	714	175	210	83.3%	16.9%	7.15	95.6
1.20	903	226	287	78.7%	15.7%	6.80	97.2
1.10	1602	378	458	82.5%	18.9%	6.35	94.9
1.05	928	227	276	82.2%	21.3%	5.39	95.4
1.00	928	234	325	72.0%	25.1%	4.34	92.4
Total	8117	1972	2464	80.0%	14.6%	7.20	98.3

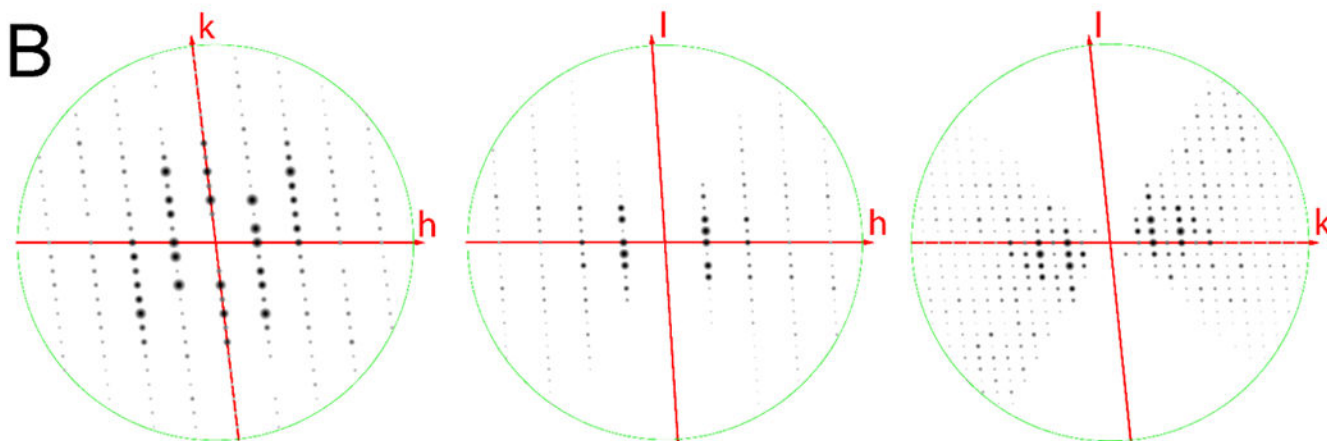


Figure 4.

Data reduction statistics for the merging and scaling of partial datasets from 6 peptide crystals (A). This example demonstrates reduction of data in the lowest symmetry space group, P1. The lack of symmetry is confirmed by a lack of systematic absences along hkl zones of the merged and scaled data (B; l=0 left, k=0 middle, h=0 right) in ViewHKL.

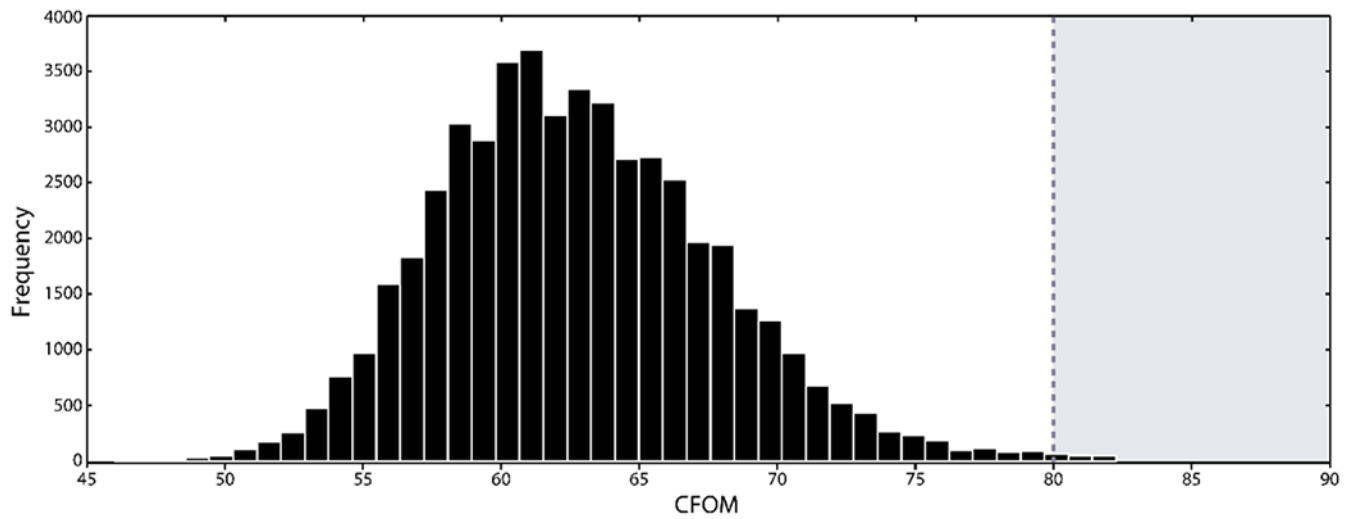


Figure 5. Histogram of the combined figure of merit (CFOM) scores for 50,000 trials by SHELXD, indicating the approximate frequency of correct solutions. The shaded region, where CFOM scores exceed 80 (6), represents an area in which solutions have a high probability of being correct.

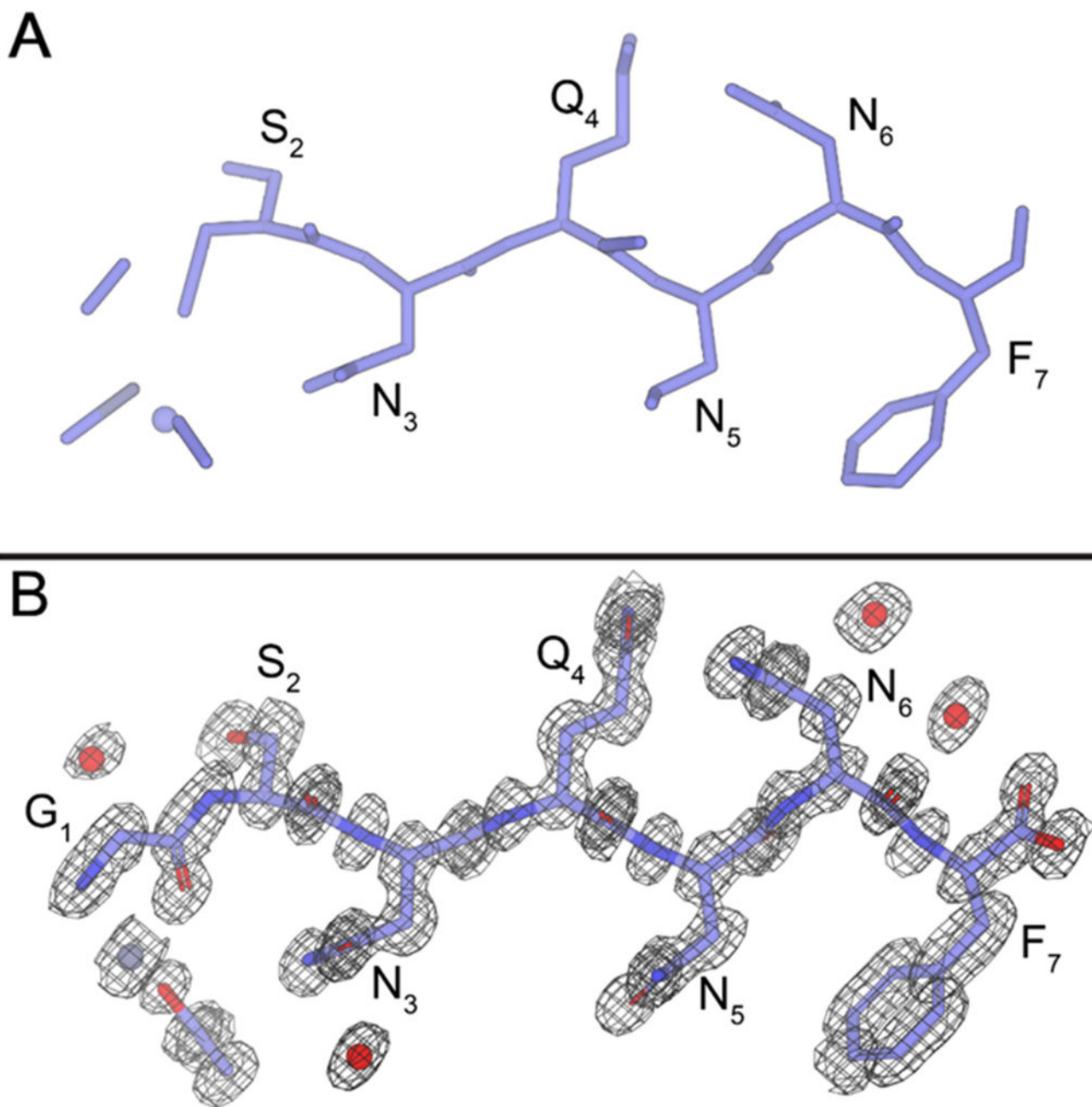


Figure 6. *Ab initio* atomic coordinates of L-GSNQNNF outputted by SHELXD (A) and the corresponding atomic coordinates refined by Phenix (B). The 2F_o-F_c map, represented by the black mesh, is contoured at 1.2 σ. Modelled water molecules are present as red spheres, with hydrogens omitted for clarity. The final structure has an R_{work} of 0.172 and an R_{free} of 0.205.

Table 1.

Relativistic and non-relativistic electron wavelengths at energies used in MicroED experiments (41).

Accelerating voltage (keV)	Non-relativistic wavelength (Å)	Relativistic wavelength (Å)	Percent error
100	0.0386	0.0370	4.15%
120	0.0352	0.0335	4.83%
200	0.0273	0.0251	8.06%
300	0.0223	0.0197	11.66%
400	0.0193	0.0164	15.03%

Author Manuscript

Author Manuscript

Author Manuscript

Author Manuscript